

See discussions, stats, and author profiles for this publication at: <https://www.researchgate.net/publication/230550279>

Merocyanine/C60 Planar Heterojunction Solar Cells: Effect of Dye Orientation on Exciton Dissociation and Solar Cell Performance

ARTICLE *in* ADVANCED FUNCTIONAL MATERIALS · JANUARY 2012

Impact Factor: 11.81 · DOI: 10.1002/adfm.201101697

CITATIONS

40

READS

53

14 AUTHORS, INCLUDING:



Antti Ojala

VTT Technical Research Centre of Finland

8 PUBLICATIONS 118 CITATIONS

SEE PROFILE



Annemarie Pucci

Universität Heidelberg

193 PUBLICATIONS 2,246 CITATIONS

SEE PROFILE



Thomas Kirchartz

Forschungszentrum Jülich

92 PUBLICATIONS 1,975 CITATIONS

SEE PROFILE

Merocyanine/C₆₀ Planar Heterojunction Solar Cells: Effect of Dye Orientation on Exciton Dissociation and Solar Cell Performance

Antti Ojala, Andreas Petersen, Andreas Fuchs, Robert Lovrincic, Carl Pölking, Jens Trollmann, Jaehyung Hwang, Christian Lennartz, Helmut Reichelt, Hans Wolfgang Höffken, Annemarie Pucci, Peter Erk, Thomas Kirchartz, and Frank Würthner*

In this study the charge dissociation at the donor/acceptor heterointerface of thermally evaporated planar heterojunction merocyanine/C₆₀ organic solar cells is investigated. Deposition of the donor material on a heated substrate as well as post-annealing of the complete devices at temperatures above the glass transition temperature of the donor material results in a twofold increase of the fill factor. An analytical model employing an electric-field-dependent exciton dissociation mechanism reveals that geminate recombination is limiting the performance of as-deposited cells. Fourier-transform infrared ellipsometry shows that, at temperatures above the glass transition temperature of the donor material, the orientation of the dye molecules in the donor films undergoes changes upon annealing. Based on this finding, the influence of the dye molecules' orientations on the charge-transfer state energies is calculated by quantum mechanical/molecular mechanics methods. The results of these detailed studies provide new insight into the exciton dissociation process in organic photovoltaic devices, and thus valuable guidelines for designing new donor materials.

1. Introduction

Progress in the field of organic photovoltaics (OPV) has been rapid in recent years and cell efficiencies approaching 8%^[1] have been reported. However, to further increase the efficiency beyond 10%, which is generally considered as the watershed for a wider commercialization of the concept, a deeper understanding of the correlation between molecular level processes and the cell performance is needed.^[2] One of the key processes in OPV cells and also the major difference compared to inorganic techniques concerns the formation of free charge carriers. In organic solar cells the absorption of a photon leads to the formation of a strongly bound electron-hole pair, known as an exciton. Since the built-in electric field of the device is insufficient to dissociate the excitons, they have to travel to

a heterointerface between donor (D) and acceptor (A) components where the local energy level offset supports the dissociation. According to studies with polymer/fullerene blends, the dissociation of an exciton into free electron-hole pair takes place via an intermediate charge transfer (CT) state (D⁺/A⁻) in which the electron and hole are located on the lowest unoccupied molecular orbital (LUMO) of an acceptor molecule and on the highest occupied molecular orbital (HOMO) of the adjacent donor molecule, respectively.^[3] At this point, the closely bound electron-hole pair is assumed to experience a strong Coulomb binding and can either dissociate into free charges or geminately recombine back to the ground state.^[4] Several studies have identified geminate recombination as one of the main loss mechanism in OPV.^[3c,5] It is widely accepted that a sufficient energy offset $\Delta E_{\text{LUMO}} = E_{\text{LUMO}}^{\text{D}} - E_{\text{LUMO}}^{\text{A}}$ between the LUMO levels of donor and acceptor materials is needed to provide the driving force for the CT-state dissociation.^[3a,3b,6] On the other hand, the open circuit voltage V_{OC} of the organic planar and bulk heterojunction solar cells has been shown to be ultimately limited by the HOMO/LUMO energy level offset at the interface of donor and acceptor molecules.^[7] Therefore, ΔE_{LUMO} has

A. Ojala, Prof. F. Würthner
Institut für Organische Chemie und Röntgen
Research Center for Complex Material Systems
Universität Würzburg
Am Hubland, 97074 Würzburg, Germany
E-mail: wuerthner@chemie.uni-wuerzburg.de



A. Ojala, A. Fuchs, Dr. C. Lennartz, Dr. H. Reichelt, Dr. J. Hwang,
Dr. H. W. Höffken, Dr. P. Erk
BASF SE, Carl-Bosch-Straße 38, 67056 Ludwigshafen, Germany

A. Petersen
Robert Bosch GmbH, Robert-Bosch-Platz 1
70839 Gerlingen-Schillerhöhe, Germany

Dr. R. Lovrincic,^[+] C. Pölking, J. Trollmann, Prof. A. Pucci
Kirchhoff-Institut für Physik der Universität Heidelberg
Im Neuenheimer Feld 227, 69120 Heidelberg, Germany

Dr. T. Kirchartz
Blackett Laboratory of Physics
Imperial College
South Kensington, London SW7 2AZ, UK

[+] Present address: Department of Materials and Interfaces, Weizmann
Institute of Science, 76100 Rehovot, Israel

DOI: 10.1002/adfm.201101697

to be optimized in order to maximize V_{OC} and at the same time provide a sufficient driving force for the CT-state dissociation.

In polymer/fullerene^[8] bulk heterojunction (BHJ) devices and planar heterojunction (PHJ) phthalocyanine (Pc)/dicyanovinyl-terthiophene (DCV)^[9] and Pc/fullerene^[7d] cells, an efficient CT-state dissociation has been observed for an energy offset of ~ 0.4 eV. However, very recently, Gong et al.^[10] demonstrated modest OPV performance with a poly(3-hexylthiophene) (P3HT)/12-(3,6-dimethoxy-fluoren-9-ylidene)-12*H*-dibenzo[*b,h*]fluorine blend, which shows a LUMO level offset of only 0.12 eV.

The current–voltage (J – V) characteristics of PHJ solar cells often deviate from an ideal diode behavior which results in low fill factor (FF). This behavior has been attributed mainly to the following reasons: i) imbalanced charge carrier mobilities and a high series resistance,^[11] ii) low effective electric field at the heterointerface,^[12] and iii) accumulation of charges at the electrodes due to interface trapping.^[13] The low FF can be significantly improved by inducing crystallization^[12] or doping of the semiconductors^[14] and thus improve the transport properties of the devices. Molecular orientation at the heterointerface may also play a significant role in the exciton dissociation process as recently discussed in theoretical studies with pentacene/ C_{60} ^[15] and P3HT/ C_{60} ^[16] interfaces.^[17] Additionally, depending on the alignment of the molecules' dipole moment at the heterointerface with respect to the applied field, the charge dissociation might be either supported or hindered.^[3d,18]

Interestingly, with highly dipolar merocyanine dyes excellent results have recently been obtained in both solution and vacuum deposited bulk heterojunction (BHJ) solar cells.^[19] This was achieved, despite the relatively narrow band gap (~ 2.1 eV), owing to exceptionally high V_{OC} (1.0 V) and J_{SC} values (up to almost 12 mA cm^{-2}), whereas low FF of $< 40\%$ for solution-processed and $< 50\%$ for vacuum-processed devices pinpoint the drawback that needs to be further analyzed.^[19b]

In this study, we investigate PHJ and BHJ merocyanine/ C_{60} solar cells deposited by thermal evaporation. Current–voltage (J – V) characteristics of as-deposited devices show a strong dependence on the applied voltage. The application of thermal treatment steps during the fabrication process significantly diminishes this voltage dependence. We show that the origin of the low FF of the as-deposited cells is the initially low exciton dissociation efficiency at the D/A heterointerface. It dramatically improves during post-annealing above the glass transition temperature of the merocyanine dye. An ellipsometric analysis reveals that the preferred orientation of the donor molecules undergoes a change upon annealing. Based on this result, two heterointerface models are simulated and their charge transfer (CT) exciton energies are calculated. These results support the experimental observation that the orientation of the dye molecules at the heterointerface has a significant influence on the exciton dissociation efficiency.

2. Results and Discussion

2.1. Energy-Level Diagram

The molecular structures of the employed donor and acceptor materials and the energy level diagram of the PHJ cells are

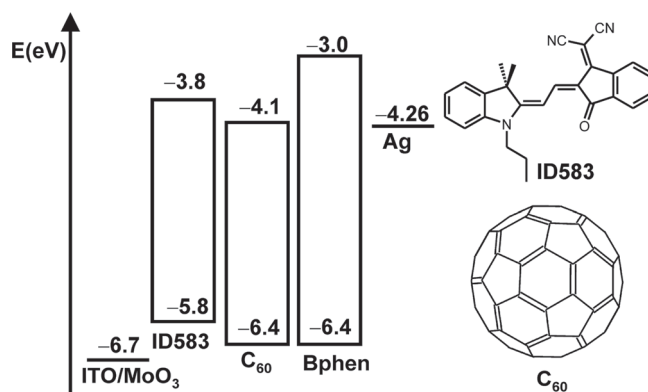


Figure 1. Energy level diagram and molecular structures of the donor (ID583) and acceptor (C_{60}) materials.

depicted in Figure 1. The HOMO level of ID583 was obtained from a cyclic voltammetric (CV) measurement and the LUMO position was estimated by adding the optical band gap [λ_{max} (as-deposited thin film) = 605 nm] to the HOMO energy. The HOMO and LUMO values of ID583 are -5.81 and -3.76 eV, respectively. A commonly used HOMO value for C_{60} (obtained by ultraviolet photoelectron spectroscopic (UPS) analysis) is -6.4 eV ^[7c,20] whilst different values for the LUMO level have been proposed.^[20a,21] In this study, a value of -4.1 eV ^[21b] (obtained by an inverse photoemission spectroscopic method) is assumed as the LUMO level of C_{60} . The energy levels for MoO₃, Bphen, and Ag are taken from literature.^[22]

2.2. Device Characteristics

The device architecture of planar heterojunction (PHJ) cells comprises: ITO/MoO₃ (5 nm)/ID583 (7–28 nm)/ C_{60} (35 nm)/Bphen (5 nm)/Ag (100 nm) where the ID583 layer thickness was varied in steps of 7 nm from 7–28 nm. Figure 2a depicts the J – V characteristics of the illuminated PHJ cells with four different donor layer thicknesses. Table 1 summarizes their key device parameters. At negative applied voltage ($V < 0$ V), all cells with different thickness of the donor layer show a very similar and well saturated photocurrent indicating an efficient extraction of free charge carriers. The high leakage current of the 7 nm donor film device at the high reverse voltage region ($V < -0.4$ V) is attributed to the low parallel resistance of the cell. When biased in forward direction ($V > 0$ V), the cells with the 14, 21, and 28 nm donor layers show a kink after which the photocurrent starts to decline linearly, until just before the open circuit voltage (V_{OC}) condition a second kink appears due to the exponential increase of the diode current. The formation of the kinks adversely affects the performance of the devices featuring a donor layer thickness of 14, 21, and 28 nm. Their FFs have been measured to be 52, 39, and 28%, respectively. The kinks are not observed, however, in the J – V curve of the thinnest cells (7 nm donor layer) which yields the highest fill factor (FF) of 69%. Notably, the exceptionally high V_{OC} (1.04–1.07 V) and the short circuit current (J_{SC}) are not affected by the kinks. The best J_{SC} (5.4 mA cm^{-2}) is observed for the cells with a donor layer

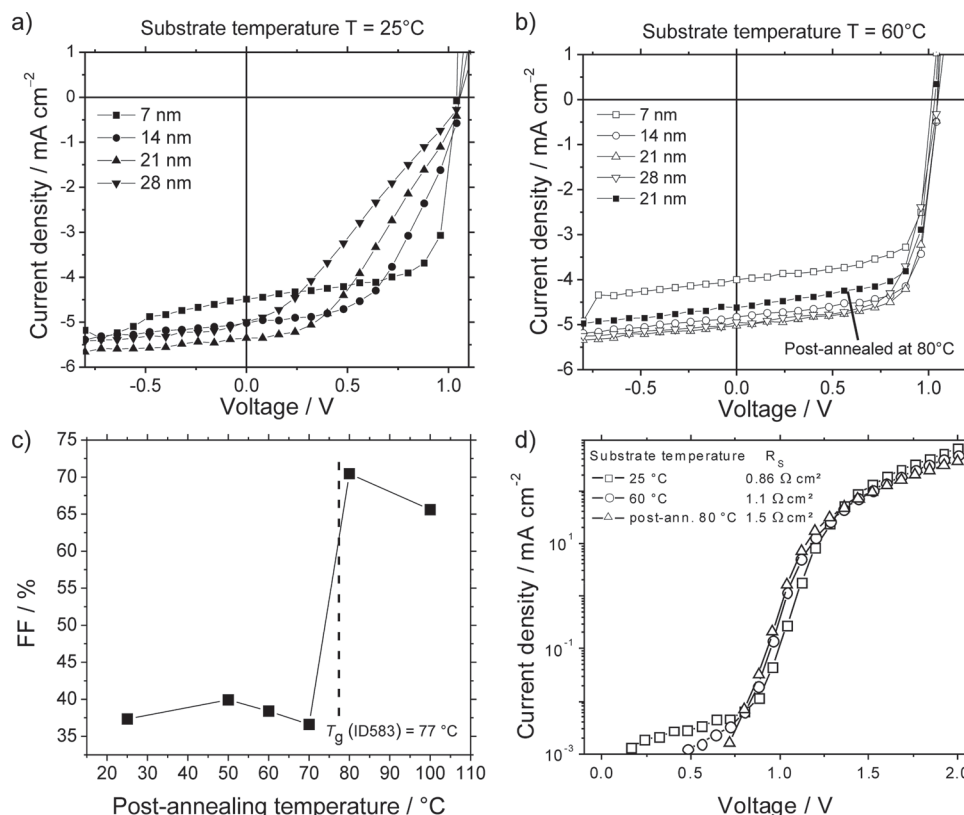


Figure 2. *J*–*V* characteristics of the PHJ cells prepared at substrate temperatures of a) 25 °C and b) 60 °C with four different ID583 layer thicknesses. c) Dependence of the FF of PHJ devices with 21 nm thick donor layers on the post-annealing temperature. The glass-transition temperature (T_g) of ID583 is illustrated by the dashed line. The solid lines are to guide the eye. d) Forward dark *J*–*V* characteristics of the PHJ cells (21 nm donor film) after different heat treatments. Series resistance (R_s) is estimated by the slope (dV/dJ) at voltage range close to $V = 2$ V.

thicknesses of 21 nm. However, due to the rapidly decreasing FF upon increasing the layer thickness, the cells with the thinnest (7 nm) donor layers give the highest power conversion efficiency (PCE) of 3.2%.

Figure 2b shows the *J*–*V* characteristics of PHJ cells deposited on a preheated (60 °C) substrate. Interestingly, these devices do not exhibit similar kinks as the cells prepared at 25 °C. Therefore, the FF of the cells with the 14, 21, and 28 nm donor layers is significantly improved to 72, 70, and 64%, respectively. The enhancement of the FF is especially high for the thickest cell

that showed a 2.2-fold increase compared to a corresponding as-deposited device. Preheating of the substrate does not influence the V_{OC} (1.04 V) but J_{SC} is slightly reduced, which is attributed to the lower absorption strength of the ID583 films evaporated on a preheated substrate (see the Supporting Information). However, due to the significantly improved FF, the optimal donor layer thickness is increased from 7 to 21 nm, which yielded a PCE of 3.9%, which is among the highest values achieved to date for vacuum-deposited PHJ devices.^[12b,23]

Additionally, completely manufactured PHJ cells with a 21 nm thick donor layer were tempered on a hot plate at 50, 60, 70, 80, and 100 °C for 5 min. Interestingly, post-annealing of the cells at temperatures of 50, 60 and 70 °C has a negligible or even slightly negative influence on cell performance while annealing the cells at 80 °C almost doubles the FF from 37 to 70% (Figure 2c). The reason for the significantly improved FF is the disappearance of the kinks in the *J*–*V* characteristics (Figure 2b). The V_{OC} of the post-annealed (80 °C) devices is 1.04 V but due to a reduced J_{SC} (4.5 mA cm^{−2}), PCE (3.3%) remained below the value obtained on a preheated substrate. Post-annealing of ID583 neat films at 80 °C reduces the absorption strength and

Table 1. Key device characteristics of the PHJ and BHJ devices.

Fabrication temp. [°C]	Cell type	Donor layer thickness [nm]	J_{SC} [mA cm ^{−2}]	FF [%]	V_{OC} [V]	PCE [%]
25	PHJ	7	4.5	69	1.04	3.2
25	PHJ	14	5.0	52	1.06	2.8
25	PHJ	21	5.4	39	1.07	2.3
25	PHJ	28	5.0	28	1.07	1.5
80 ^{a)}	PHJ	21	4.5	70	1.04	3.3
60 ^{b)}	PHJ	21	5.2	70	1.06	3.9
25	BHJ	28 ^{c)}	7.5	55	1.00	4.1

^{a)}Post-annealed; ^{b)}Heated substrate; ^{c)}ID583:C₆₀ (40:60 weight ratio) layer.

shifts the maximum to slightly smaller wavelength ($\lambda_{\text{max}} = 595 \text{ nm}$) compared to the as-deposited film ($\lambda_{\text{max}} = 605 \text{ nm}$). The decreased J_{SC} of the post-annealed devices is mainly attributed to the reduced absorption strength. However, possible changes in the thermally instable Bphen layer ($T_g = 62 \text{ }^\circ\text{C}$)^[24] or the exciton diffusion length of the ID583 layer cannot be excluded. Increasing the temperature to $100 \text{ }^\circ\text{C}$ does not further improve the device performance; instead a small decline was observed in all cell parameters compared to post-annealing at $80 \text{ }^\circ\text{C}$.

2.3. Dye and Film Properties

In order to understand the behavior of the PHJ devices, especially the sudden improvement of the FFs after post-annealing at $80 \text{ }^\circ\text{C}$, we applied different analytical methods. First, the thermal properties of a ID583 powder sample were analyzed by differential scanning calorimetric (DSC) method (see the Supporting Information). Heating of an amorphous sample of ID583 (prepared by fast cooling from the melt) reveals an endothermic step in the base line at $77 \text{ }^\circ\text{C}$, which is attributed to the glass transition temperature (T_g) of the material. Additionally, an exothermic crystallization peak and endothermic melting characteristics have been observed at 141 and $221 \text{ }^\circ\text{C}$, respectively. Hence the T_g is observed at the same temperature region where the post-annealing significantly improves the FF of the PHJ devices (see Figure 2c).

Changes of the film morphology were investigated by atomic force microscopy (AFM). Two samples with 21 nm ID583 neat films were evaporated on ITO/MoO₃ (5 nm) covered glass slides at substrate temperatures of 25 and $60 \text{ }^\circ\text{C}$. The ID583 films deposited at $25 \text{ }^\circ\text{C}$ show a root-mean-square (RMS) roughness of 0.84 nm whereas the films deposited at $60 \text{ }^\circ\text{C}$ have a significantly lower roughness of 0.62 nm (for AFM figures see the Supporting Information). Additionally, X-ray powder diffraction (XRPD) patterns were recorded for ID583 neat films prepared at 25 and $60 \text{ }^\circ\text{C}$ or post-annealed at $80 \text{ }^\circ\text{C}$ (see the Supporting Information). No coherent reflections arising from the ID583 layers have been observed. This, together with the AFM results (decreasing roughness at elevated deposition temperatures), suggests that the films are X-ray amorphous.

In a recent study on small molecule PHJ solar cells anomalous J - V characteristics were attributed to imbalanced charge carrier mobilities between the donor and acceptor layers.^[11] This possibility in our devices was explored by measuring the hole mobilities of the ID583 hole-only devices prepared under different thermal conditions and by applying a space-charge-limited-current (SCLC) model (see the Supporting Information).^[25] The hole mobility of the devices fabricated at $25 \text{ }^\circ\text{C}$ is $6 \times 10^{-6} \text{ cm}^2 \text{ V}^{-1} \text{ s}^{-1}$, whereas the deposition at $60 \text{ }^\circ\text{C}$ or post-annealing at $80 \text{ }^\circ\text{C}$ yields only 2×10^{-6} and $6 \times 10^{-7} \text{ cm}^2 \text{ V}^{-1} \text{ s}^{-1}$, respectively. The previously reported electron mobility of C₆₀ is approximately $10^{-2} \text{ cm}^2 \text{ V}^{-1} \text{ s}^{-1}$.^[26] Obviously, the decrease in hole mobilities with increased deposition temperature or with thermal annealing cannot explain the cause of the improved FFs in our PHJ devices. Consistently with the experimental hole mobilities, also the series resistance (R_s) of the PHJ cells with a 21 nm thick ID583 layer gets worse after the thermal treatments (Figure 2d). Devices prepared at $25 \text{ }^\circ\text{C}$ show the lowest

R_s of $0.86 \text{ } \Omega \text{ cm}^2$ whilst the highest R_s of $1.5 \text{ } \Omega \text{ cm}^2$ is observed for the post-annealed ($80 \text{ }^\circ\text{C}$) devices. Depositing the cells at $60 \text{ }^\circ\text{C}$ results in an intermediate value ($R_s = 1.1 \text{ } \Omega \text{ cm}^2$). Note, that FFs of the devices prepared at 25 and $60 \text{ }^\circ\text{C}$ or post-annealed at $80 \text{ }^\circ\text{C}$ were 39 , 70 , and 70% , respectively.

2.4. Analytical Electric Field Dependent CT-State Dissociation Model

As discussed above and depicted in Figure 2a, the onset of the kinks in the J - V characteristics of the as-deposited PHJ cells gradually shifts to lower applied voltages with increasing donor layer thickness. By calculating the inverse of the slopes between the kinks and plotting them against the corresponding donor layer thicknesses, a linear correlation is observed (see the Supporting Information). This correlation is directly reflected in the FF of the devices which also linearly declines as the device thickness increases. These findings strongly suggest that the photocurrent at voltages around the maximum power point (mpp) depends on the effective electric field that can be approximated by

$$F_{\text{el}} = \frac{(V - V_{\text{bi}})}{d} \quad (1)$$

where $d = d_{\text{donor}} + d_{\text{acceptor}}$ is the total cell thickness. The applied and the built-in voltage are labeled V and V_{bi} , respectively. In previous studies, the strong field dependence has been attributed to a high series resistance^[11] or to a low exciton dissociation efficiency at the D/A heterointerface.^[12]

Since it was found that the hole mobility and thus the charge transport properties of the donor material did not improve and even slightly decline during thermal treatment, the R_s cannot be the cause of the low FF and high field dependency of the as-deposited (substrate temperature $T = 25 \text{ }^\circ\text{C}$) PHJ cells. Furthermore, the field dependency cannot be attributed to non-geminate recombination since we have a planar heterojunction structure. In order to analyze the charge dissociation efficiency at the heterointerface, a field-dependent CT-state dissociation model has been used to describe the illuminated J - V characteristics of the as-deposited devices. Within the frame of this model the current is given by

$$J(V) = J_{\text{dark,exp}}(V) - J_{\text{photo}}(V) \quad (2)$$

where $J_{\text{dark,exp}}(V)$ is the measured current of the not illuminated cell and the voltage dependent photocurrent is given by

$$J_{\text{photo}}(V) = p(V)J_{\text{photo,sat}} \quad (3)$$

Here $J_{\text{photo,sat}}$ is the saturation value of the photocurrent and $p(V)$ denotes the voltage dependent CT-state dissociation probability which can be calculated from the CT-state dissociation rate $k_{\text{diss}}(V)$ and its recombination rate k_f

$$p(V) = \frac{k_{\text{diss}}(V)}{k_{\text{diss}}(V) + k_f} = \frac{1}{1 + \frac{k_f}{k_{\text{diss}}(V)}} \quad (4)$$

This expression assumes a finite lifetime of the CT-state $\tau = k_f^{-1}$ with respect to recombination and was introduced by Braun.^[27] The CT-state dissociation rate is expressed as^[28]

$$k_{\text{diss}}(V) = k_{\text{diss},0} \frac{\left[1 - \exp\left(\frac{-q F_{\text{el}} r_s}{k_B T}\right)\right]}{q F_{\text{el}} r_s} k_B T \quad (5)$$

where $k_{\text{diss},0}$ is the dissociation rate at zero field, k_B and T are the Boltzmann constant and the temperature, respectively, and r_s is the distance over which the electric field is acting on the CT-state. This distance is the difference between the initial electron-hole pair separation in the CT-state and the distance at which the two charge carriers can be considered free. We use r_s as a fitting parameter. A more detailed discussion of the model will be published elsewhere.^[28]

Using the loss ratio k_r/k_{diss} and the separation distance r_s as free parameters, the exciton dissociation model is fitted to the J - V characteristics of the illuminated as-deposited PHJ cells. **Figure 3** shows the excellent agreement of the model and the experimental data. The parameters used in the simulation are given in the Supporting Information. The well saturated current densities at the applied voltage region of $V < 0$, imply an efficient CT-state dissociation in all devices. However, when the direction of the applied electric field is reversed ($V > 0$), the CT-state separation probability $p(V)$ decreases notably. For cells with a nominal donor layer thickness of 14 nm and at $V = 0.5$ V, the model predicts a separation probability of $p = 89\%$ while the cells with a 21 nm donor layer only reach about 76%, at the same value of the applied voltage V . Furthermore, when the nominal donor layer thickness increases to 28 nm, the predicted probability for the CT-state dissociation at $V = 0.5$ V is only 62%. Since the internal field decreases with increasing cell thickness, the concurrent decrease of the field-assisted separation probability is a strong indication of the photocurrent being controlled by a geminate recombination process. Thus, the formation of kinks around the mpp of the as-deposited solar cells may be attributed to the high recombination rates of the geminately bound electron-hole pairs (CT-states).

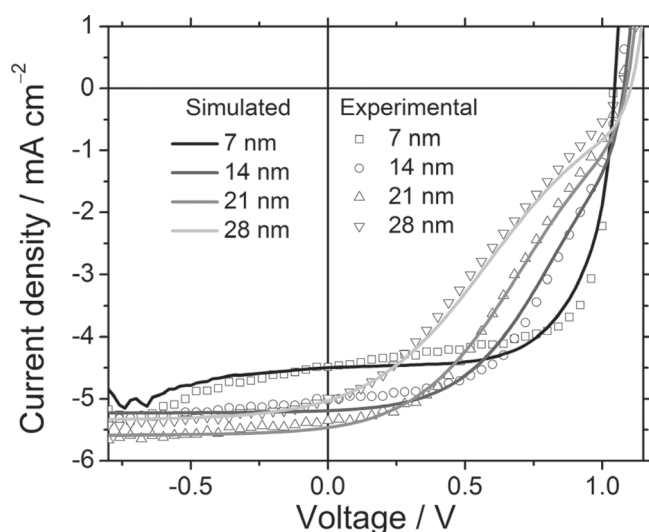


Figure 3. Experimental (symbols) and simulated (solid lines) J - V characteristics of PHJ cells with different donor layer thicknesses. The simulated curves are calculated according to Equation 3 using the parameters shown in the Supporting Information.

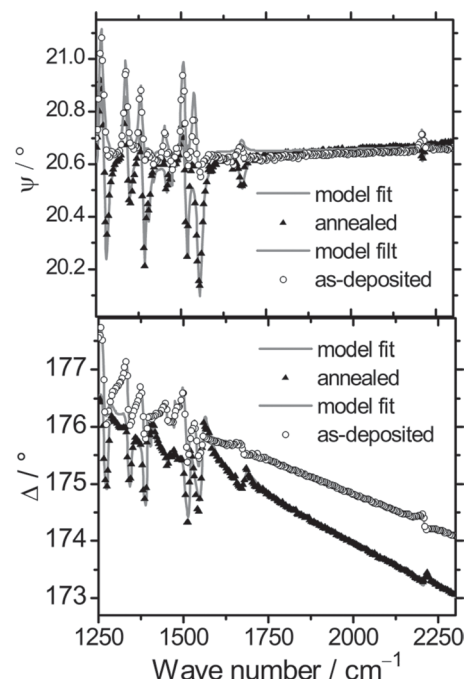


Figure 4. Measured ellipsometric parameters (symbols) Ψ and Δ for an as-deposited and annealed film on $\text{MoO}_3/\text{SiO}_2/\text{Si}$ substrates, and the corresponding modeled spectra (continuous lines). The ID583 films (thicknesses around 30 nm) were modeled as optically uniaxial (see the Supporting Information for details).

2.5. Molecular Orientations as Deduced from Infrared Spectroscopic Ellipsometry

The XRPD measurements indicate that the amorphous ID583 neat films did not crystallize upon evaporation at elevated substrate temperatures or at post-annealing above the T_g of the dye. However, it is well known that organic films may possess different degrees of order, although the size of the ordered regions is too small to give coherent reflections in XRPD (X-ray amorphous). Therefore, we have performed infrared spectroscopic ellipsometry (IRSE) analysis for two types of samples: thin films of ID583 (28 nm) evaporated on $\text{Si}/\text{SiO}_2/\text{MoO}_3$ with and without post-annealing at 80 °C for 5 min. In all cases the thicknesses of the MoO_3 and the natural Si oxide have been found to be around 3 nm. **Figure 4** shows the ellipsometric parameters obtained from both sample types at an angle of incidence of $\theta = 60^\circ$ (see the Supporting Information for results at $\theta = 75^\circ$) and the corresponding modeled spectra (see the Supporting Information for details on the IRSE modeling). Already the raw data reveal clear indications for a change of molecular orientation upon annealing. Thus, the peak at 2209 cm^{-1} ($\nu_{\text{C-N}}$) is a dip-down in Ψ for the annealed film and a dip-up for the as-deposited film, corresponding to out-of-plane and in-plane vibrations, respectively.^[29] For a precise determination of the structural change in the film upon annealing, the accordance between the modeled dielectric function and the DFT (BP86/SV(P) level of theory) predicted absorption intensities was optimized by rotating a basis molecule set (and thereby the dipole moments) relative to the substrate. For each

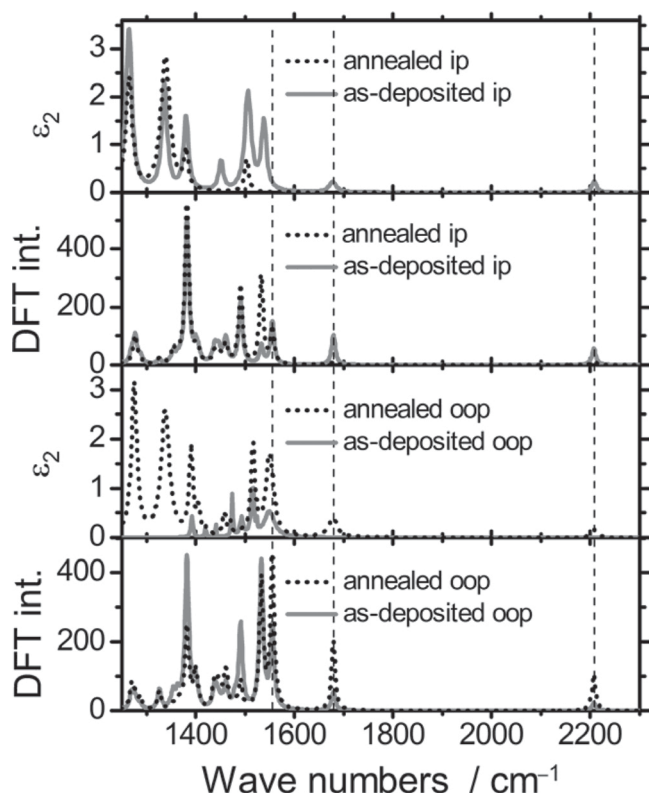


Figure 5. In-plane (ip) and out-of-plane (oop) contributions of ϵ_2 and the absorption peaks calculated by DFT. Fitting of DFT (BP86/SV(P) level of theory) based intensities to the experimental results was performed by using the three peaks marked with broken lines.

orientation a figure of merit (rating) was computed, and the orientation with best rating is then regarded as the preferred orientation of the molecules (see the Supporting Information for details). The optimization process was performed on three pronounced peaks at 1555 ($\delta_{\text{C-H}}$), 1678 ($\nu_{\text{C-O}}$), and 2209 cm^{-1} ($\nu_{\text{C-N}}$). **Figure 5** shows the experimentally derived imaginary parts ϵ_2 of the dielectric functions for the two direction components of each sample in comparison to DFT intensity predictions for the optimized orientations of the molecule. As can be seen in **Figure 6**, the result indicates that in the as-deposited film the molecules are preferably standing with their long axis perpendicular to the substrate surface, and undergo a tilt of 45° upon annealing at 80 °C. This change is certainly driven by a higher packing density for the tilted orientation. As no peaks were observed in X-ray diffraction measurements for both annealed and non-annealed films, it can be concluded that the films are X-ray amorphous but the molecules tend to align their long molecular axes along certain directions, namely along the surface normal in as-deposited films and along 45° relative to the surface normal after annealing.

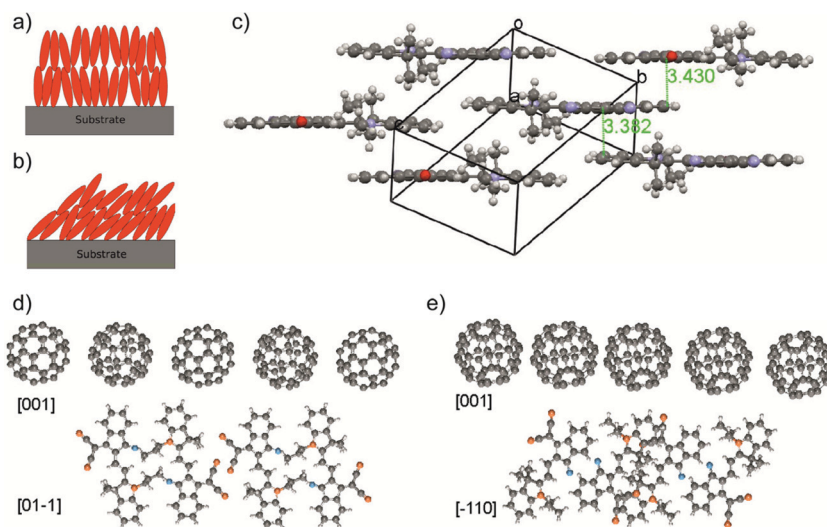


Figure 6. Schematics of the dye molecules' orientations before (a) and after (b) annealing at 80 °C deduced from the ellipsometric analysis. c) A brick wall packing motif in the single crystal structure of ID583. The shortest atom-to- π -plane distances are also shown. Schematics of the interfaces ID583[01-1]:C₆₀[001] (d) and ID583[-110]:C₆₀[001] (e).

2.6. Computations of the CT-State Energies at the ID583/C₆₀ Interface

The kinks disappear and the fill factors significantly improve when substrate heating is applied or the devices are post-annealed at 80 °C which is just above the T_g (77 °C) of the dye. The fact that the post-annealing below the T_g has negligible influence on the device performance strongly suggests that the reorientation of the dyes, as shown by the IRSE spectroscopic analysis, is the key for the improved device performance. In a recent theoretical^[15] study with pentacene/C₆₀ PHJ cells, it was observed that changes on the relative orientation of the quadrupolar donor molecule at the D/A interface have a significant influence on the charge dissociation energetics. Exposing the negatively charged π -plane of the pentacene to the C₆₀ interface was found to give an additional driving force for the exciton dissociation. Unlike pentacene, ID583 contains a donor-acceptor π -conjugated molecular scaffold with a permanent ground state dipole moment (7.1 D along the long and 5.5 D along the short axis of the molecule on BP86/TZVP level of theory).^[30] Upon optical excitation of such push-pull chromophores the electron density is even further displaced toward the acceptor part of the dye leading to even larger dipole moments in the excited state.^[31] Therefore, the relative orientation of molecules close to or at the D/A interface can have a significant impact on stabilization of the electron-hole pair and its dissociation at the interface.^[15]

To assess the influence of the dyes' orientation on the stabilization of the electron-hole pair in the ID583/C₆₀ cells, two model interfaces were built using the crystal structures of C₆₀ and ID583. In order to create meaningful interface structures, the preferred orientations from the IRSE study were compared with the single crystal structure of ID583 (**Figure 6c**). It is obvious that the perpendicular orientation of the long molecular axis of ID583 in the as-deposited films and the tilted (45°) arrangement after annealing match very well with the lattice

Table 2. Energy of the CT-state for different bimolecular ID583/C₆₀ interface configurations.

Interface	Exposed side of the dye	$E(\text{CT})$ [eV]	$\Delta G_{S_1 \rightarrow \text{CT}}$ [eV] ^{a)}	Configuration
[−110]:[001]	Acceptor	1.54	−0.51	2A
[−110]:[001]	Donor	1.95	−0.10	2D
[01−1]:[001]	Acceptor	1.35	−0.70	1A
[01−1]:[001]	Donor	1.61	−0.45	1D

^{a)}The driving force between the measured optical gap (S₁) of ID583 (2.05 eV) and the calculated energy of the CT-state.

planes [01−1] and [−110], respectively. Therefore, the interface models ([01−1]:[001] and [−110]:[001]) were constructed by positioning the C₆₀ plane [001] over the dye layers. The distances between the layers were optimized using the Dreiding-force field^[32] (Figure 6). All other degrees of freedom (intramolecular relaxation, translation and rotation of the molecules) were kept fixed. Note, that the space group of the crystal structure of ID583 is centrosymmetric P-1 having two molecules with antiparallel orientation of the long molecular axis in the unit cell. We expect the antiparallel orientation of ID583 also to be found at the interface of the planar heterojunction. Therefore, two different types of interfaces with clearly distinct contacts between the merocyanine and fullerene components must be considered: One where the acceptor part (indane) of the ID583 dye molecule is exposed to the C₆₀ surface (in the following called A configurations) and one where the dyes' donor part (indoline) is exposed (in the following called D configurations). A detailed description of the simulations can be found in the Supporting Information.

The energy of the charge transfer exciton for the different bimolecular (ID583/C₆₀) interface configurations is shown in **Table 2**. **Figure 7** demonstrates the energy-level diagram of the ID583/C₆₀ interface with energy levels of the different electron–hole pairs at the perpendicular and tilted interfaces. The energy levels of the electron–hole pairs are given relative to the HOMO energy of ID583. As expected, the energy of the CT-state critically depends on the interface geometry as well as on the orientation of ID583 towards the C₆₀ surface. It is interesting to note that, irrespective of the interface geometry, the CT-state is lower in energy when the (partially negatively charged) indane acceptor group of the dye is exposed to the C₆₀ surface (configurations 1A and 2A). Due to the antiparallel orientation, the neighboring ID583 molecules of the bimolecular complexes 1A and 2A (which define the local polarization field) are oriented such that the indoline group is exposed to the C₆₀ surface. Therefore, the CT-state is stabilized by the positive partial charge of the indoline group of the neighboring ID583 molecules. Furthermore, due to the fact that the CT-state is generated by an electron transfer from the S₁-state of ID583 to the LUMO of C₆₀, the electron density distribution of the ID583 S₁-state crucially influences the energy of the CT-state. Therefore, when the vectors of the transition dipole moment of the S₀ → S₁ transition in ID583 and the transition dipole moment of the S₁(ID583) → CT excitation are oriented parallel, the electron density distribution is closer to the interface and the CT-state is

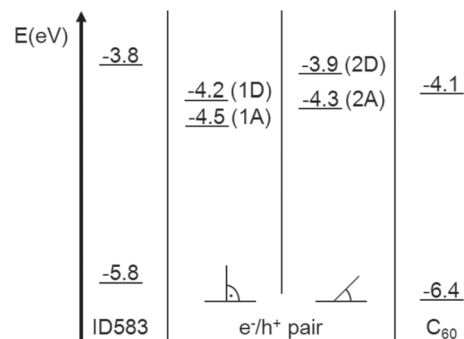


Figure 7. Energy level diagram of the ID583/C₆₀ interface with energy levels of the different electron–hole pairs at the perpendicular (second column) and tilted (third column) interfaces. D configurations refer to orientations where the dyes' donor subunit is in contact to C₆₀, A configurations refer to orientations where the dyes' acceptor subunit is in contact to C₆₀. The energy levels of the electron–hole pairs are obtained by adding the energy of the CT-state $E(\text{CT})$ (see Table 2) to the HOMO of ID583.

already preformed in the S₁-state of ID583. Hence, the CT-state at the interface can be formed more easily due to the kinetic reasons.

As can be seen in Table 2, the driving force for the formation of the CT-state, which is defined as the energy difference between the optical gap and the energy of the CT-state ($\Delta G_{S_1 \rightarrow \text{CT}} = E_{\text{CT}} - E_{\text{opt}}$), is negative for all interface configurations and relative orientations. Therefore, in principle the generation of a CT-state is possible for all four molecular orientations.

It is known from Marcus theory that the rate of charge transfer depends on the driving force.^[33] The highest rates are realized when $\Delta G_{S_1 \rightarrow \text{CT}}$ is equal to the negative reorganization energy λ of the system. The estimated λ is 0.3–0.5 eV so that the highest charge transfer rates occur at configurations 2A and 1D.^[34] Note that 2A corresponds to the low energy CT-state at the tilted interface whereas 1D is the high energy CT-state at the perpendicular interface (see Figure 7). Therefore, the electron–hole pair is expected to stay on the bimolecular ID583/C₆₀ complex 2A in the tilted case whereas the hole hops to the bimolecular complex 1A in the perpendicular case. The energy difference of 0.26 eV between the bimolecular complex 1D and 1A prevents the hole from hopping back to the other ID583 so that 1A acts as a trap state at the perpendicular interface. The rate of an electron leaving the interface can be approximated from the energy distance between the CT-state and the transport level (LUMO) of C₆₀ ($\Delta E_{\text{CT-LUMO}}^A$). Using the Marcus formula and assuming a reorganization energy λ of 0.4 eV and a transfer integral of 0.050 eV, the rate for the electron hopping from the C₆₀ molecule in configuration 2A to the bulk C₆₀ is 400 times higher (3×10^{10} Hz vs. 8×10^7 Hz) than the respective rate for the configuration 1A, which is due to the high $\Delta E_{\text{CT-LUMO}}^A$ of 0.4 eV. Note that it can be assumed that the LUMO level of the C₆₀ molecules close to the interface is different from the respective bulk level so that the electron does not need to perform the energetic jump of 0.4 eV in one step but could reach the bulk LUMO level in several smaller steps.^[15] Since this effect is expected to be similar for both interfaces, the dissociation rate of the CT-state at the tilted interface remains higher than the respective rate at the perpendicular interface. This shows that

the high energetic stabilization of the CT-state 1A (which is the global minimum of all calculated interface excitons) makes its dissociation at the perpendicular interface very unlikely. Due to the absence of an energetic trap and the lower stabilization of the exciton at the tilted interface, it is expected to show a higher exciton dissociation rate compared to the perpendicular orientation, as indicated by the CT-state dissociation simulations. Summarizing the theoretical discussion, we have demonstrated that the CT-state is stabilized when the neighboring molecules are oriented such that the positive end of ID583 is exposed to the interface. Furthermore, the exciton dissociation rate is higher when the energy difference between the interface and bulk energy level is smaller. The calculated changes of the CT-state energies, caused by the change of the molecular orientation, also agree with our CT-state dissociation model. It predicts that the driving force for the CT-state dissociation has to be increased by at least 0.1 eV in order to account for the observed device behavior.^[28] Our results are also in accordance with previous findings on merocyanine dye sensitized solar cells (DSC) which suggest that the electron injection efficiency improves if the electron accepting part of the push-pull chromophores, e.g. cyano groups, are closely located at the titanium dioxide (TiO₂) surface.^[35] Likewise, in our ID583/C₆₀ devices, the tilted orientation, in which the two cyano groups of the ID583 are closest to the C₆₀ surface, yields the highest CT-state dissociation efficiency.

2.7. Bulk Heterojunction Cells

As a comparison, we also fabricated bulk heterojunction (BHJ) cells featuring following layer structure: ITO/MoO₃ (5 nm)/ID583:C₆₀ (7–28 nm)/C₆₀ (35 nm)/BPhen (5 nm)/Ag (100 nm). The active layer thickness (ID583:C₆₀ 40:60 weight ratio) was varied from 7–28 nm in steps of 7 nm. **Figure 8** shows that the *J*–*V* characteristics of these devices do not show similar kinks as has been observed for the PHJ cells. Instead, even with the

active layer thicknesses of 28 nm, the devices exhibit high FFs of 55%. Although the open circuit voltage $V_{OC} = 1.00$ V is lower than for the PHJ cells, the PCE (4.1%) is slightly increased due to a significantly increased J_{SC} (7.5 mA cm⁻²) (for more results of devices, see the Supporting Information).

It is intriguing that the *J*–*V* characteristics of the BHJ cells resemble that of the heat-treated PHJ devices. This is explained by the different heterointerface structures of PHJ and BHJ devices. It can be assumed that the interface structure of BHJ blends is random, which leads to broad distribution of energetically different pathways for excitons to dissociate. Due to the energetically heterogeneous landscape a significant number of excitons are able to dissociate into free charges even at low effective electric field strength. In contrast, in the PHJ devices, the interface structure is expected to be more ordered leading to energetically homogenous surrounding which, depending of the dyes' relative orientation, either supports or hinders the exciton dissociation.

3. Conclusion

We have shown that by evaporating the dye film on a heated substrate or by post-annealing the complete devices above the glass transition temperature (T_g) of the donor material, we can significantly improve the FF of merocyanine/C₆₀ PHJ solar cells. By employing a field dependent charge transfer (CT) state dissociation model, we show that the low FF of the as-deposited cells is a result of the poor exciton dissociation efficiency at the D/A heterointerface which is significantly improved after the heat treatments. Although, we observe no coherent reflections in the XRPD study, the utilization of an IRSE spectroscopic analysis demonstrated that the preferred orientation of the dye molecules in the donor film changes upon post-annealing at 80 °C. Based on this finding, we simulated two D/A heterointerface models and estimated their CT-state energies via QM/MM calculations. The computations suggest that the exciton dissociation rate is higher in post-annealed devices compared to as-deposited cells. Hereby, we argue that the low exciton dissociation efficiency of as-deposited devices is a result of the unfavorable molecular orientation at the heterointerface together with an insufficient driving force (LUMO(D)-LUMO(A) offset is ~0.3 eV). However, post-annealing the devices above the T_g of the donor material changes the interface structure, facilitates the CT-state dissociation, and thus leads to a two-fold increase of the FF. Furthermore, the kinks cannot be observed in the *J*–*V* characteristics of the BHJ devices deposited at 25 °C; instead the curves resemble heat treated PHJ cells. This is due to the random orientation of the dyes at the heterointerface in BHJ devices which is expected to result in energetically favorable pathways for a significant number of excitons to dissociate.

Our comprehensive study suggests that push-pull chromophores can be beneficial for exciton dissociation at the planar and bulk heterojunction interface if they are oriented in a proper way with respect to the acceptor manifold. This finding hints that by carefully tailoring the molecular structure and/or the film morphology, the energy level alignment at the heterojunction can be further optimized. This is important, especially since dyes with pronounced charge redistributions upon

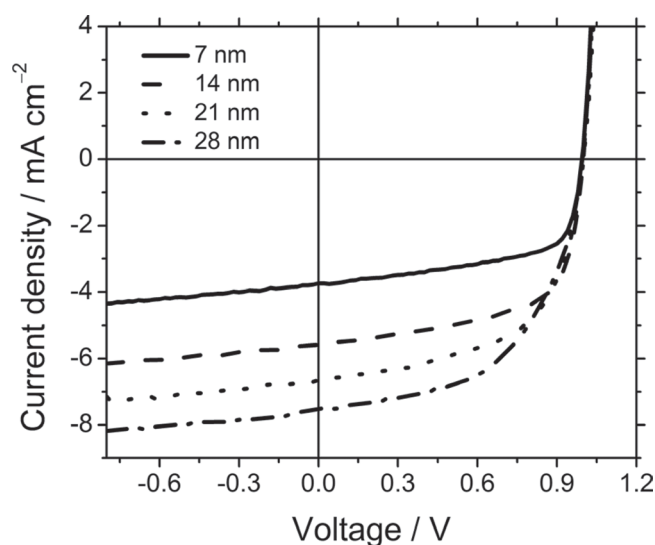


Figure 8. Illuminated *J*–*V* characteristics of BHJ devices with different ID583:C₆₀ layer thicknesses.

electronic excitation, e.g., in particular dipolar merocyanines (D-A),^[19] but also quadrupolar squaraines and diketopyrrolopyrroles (D-A-D),^[36,37] or dicyanovinyloligothiophenes (A-D-A)^[38] are increasingly utilized in organic small-molecule planar and bulk heterojunction solar cells.

4. Experimental Section

Synthesis: Merocyanine dye ID583 (1-propyl-2-[2-(3,3-trimethyl-1,3-dihydro-indol-2-ylidene)-ethylidene]-3-dicyanovinyl-indan-1-one) was synthesized by refluxing a mixture of methylene base (8.05 g, 0.04 mol), 3-dicyanovinylindan-1-one (7.76 g, 0.04 mol) and orthoformic ethyl ester (8.88 g, 0.06 mol) for 2 h in ethanol. After cooling, the crystallized product was filtered and washed with ethanol. Finally, the product was purified by recrystallizing it from dimethylformamide. Yield: 14.0 g (0.034 mol, 85%), green solid. Mp. 219–221 °C. ¹H NMR (CDCl₃, 360 MHz, δ): 9.05 (d, J = 13.6 Hz, 1H), 8.57 (m, 1H), 8.08 (d, J = 14.0 Hz, 1H), 7.72 (m, 1H), 7.59 (m, 2H), 7.36 (m, 2H), 7.25 (m, 1H), 7.07 (m, 1H), 4.04 (t, J = 7.2 Hz, 2H), 1.96 (m, 2H), 1.81 (s, 6H), 1.09 (t, J = 7.2 Hz, 3H). UV-vis (CH₂Cl₂): λ_{max} (ϵ) = 575 nm (66500 M⁻¹ cm⁻¹). Elemental analysis (%) calcd. for C₂₇H₂₃N₃O: C, 80.0; H, 5.7; N, 10.4; O, 4.0. Found: C, 80.1; H, 5.8; N, 10.4; O, 4.1.

Cyclic Voltammetry (CV): The CV measurement of ID583 was performed on a commercial electrochemical analyzer (EC epsilon; BAS Instrument, UK) in a three electrode single-compartment cell under argon. Dichloromethane (HPLC grade; J. T. Baker) was dried over calcium hydride and degassed prior to use. The supporting electrolyte tetrabutylammonium hexafluorophosphate (TBAHFP) was synthesized according to a published method.^[39] The measurements were carried out under exclusion of air and moisture at a concentration of 10⁻⁴ M with ferrocene (−5.15 eV) as internal standard for the calibration of the potential; working electrode: Pt disc; reference electrode: Ag/AgCl; auxiliary electrode: Pt wire.

Atomic Force Microscopy (AFM): The AFM experiments (Dimension 5000 Microscope, Veeco Instruments) were performed on two different 21-nm-thick ID583 films evaporated on ITO substrates at substrate temperatures of 25 and 60 °C. The measurements were carried out in the tapping mode using silicon cantilevers with a nominal force constant of 42 N/m and a tip radius of ~7 nm from Olympus, type OMCL-AC160TS (Tokyo, Japan) at a resonance frequency of about 320 kHz. The scan rate was kept at 0.7 Hz, while the tip-sample forces were carefully minimized to avoid artifacts.

Differential Scanning Calorimetry (DSC): The glass transition temperature of ID583 was measured using Q2000 (TA-instruments) differential scanning calorimeter. ID583 powder (5.4 mg) was heated/cooled at rate 20 K min⁻¹ in aluminum pan under nitrogen atmosphere.

Single-Crystal Analysis: Red block crystals of ID583 were grown by slow evaporation of a dichloromethane solution of this dye at room temperature. The diffraction data were collected at 103 K with a Bruker AXS CCD detector, using graphite-monochromated Cu K α (λ = 1.51478 Å) radiation. The structure was solved by a direct method and refined on F² using the full matrix least square method in SHELXTL program package.^[40] All non-hydrogen atoms were anisotropically refined and hydrogen atoms were placed on idealized positions. The unit cell of the analyzed crystal is a = 9.2930(10) Å, b = 9.6240(11) Å, c = 12.6184(13) Å, α = 104.859(5)°, β = 97.120(4)°, and γ = 90.374(5)°. The space group is P-1 with Z = 2. A total amount of 2067 reflections was collected with 1651 unique reflections in the range from 3.65–57.29° (2 θ). The R1 and wR1 of the refinement are 0.0354 and 0.0832, respectively. The goodness of the fit (Goof) for the solution is 1.065. Crystallographic data (excluding structure factors) for the structure reported in this paper are available at the Cambridge Crystallographic Data Centre as supplementary publication no. CCDC-834686. Copies of the data can be obtained free of charge from www.ccdc.cam.ac.uk/conts/retrieving.html or on application to the Director.

Device Fabrication: The same materials were used in all planar heterojunction (PHJ) and bulk heterojunction (BHJ) cells throughout

this work. The commercial MoO₃ (Merck), C₆₀ (CreaPhys, 2 \times sublimed), 4,7-diphenyl-1,10-phenanthroline (Bphen; Fluka) and the synthesized ID583 dye were used as received. The solar cells were manufactured in a high vacuum (typically 2 \times 10⁻⁶ mbar) chamber (Lesker Ltd) on prestructured indium tin oxide (ITO) substrates with an active cell area of 4 mm². Prior to transferring the ITO substrates into the chamber they were cleaned in UV/O₃ oven for 15 min. All PHJ devices were fabricated according to following steps: first a MoO₃ film (5 nm \pm 10%) was evaporated on the ITO substrate, followed by a 7, 14, 21, or 28 nm (\pm 10%) thick ID583 donor layer. After the ID583 film, a C₆₀ acceptor layer (35 nm \pm 10%) and a Bphen buffer film (5 nm \pm 10%) were deposited before preparation of the silver cathode (100 nm \pm 10%). The evaporation rate of all organic materials was 1.0 Å s⁻¹ whereas the MoO₃ and Ag layers were deposited at rates of 0.8 and 4 Å s⁻¹, respectively. Compared to the PHJ cells, the following changes were made in fabrication of the BHJ devices: the ID583 layers were replaced with ID583:C₆₀ (40:60 wt ratio) mixed layers with thicknesses of 7, 14, 21, and 28 nm (\pm 10%), followed by a 25 nm (\pm 10%) thick C₆₀ layer. Some of the PHJ devices were prepared on a heated substrate or post-annealed after fabrication. When substrate heating was applied, the substrate was first heated with a copper block heater to 60 °C before evaporation of the ID583 layer after which the substrate was cooled below 30 °C until the successive layers were deposited. Post-annealing of the cells was carried out such that the complete devices were heated directly after fabrication on a hot plate at 50, 60, 70, 80, and 100 °C for 5 min in nitrogen atmosphere. The current–voltage (J – V) characteristics of the cells were measured under AM 1.5G simulated illumination (Xe lamp) in ambient air and controlled by a Keithley 2425 source measurement unit. The light intensity (100 mW cm⁻²) was adjusted by a calibrated Si reference cell.

Infrared Spectroscopic Ellipsometry (IRSE): Ellipsometry measures the complex reflectance ratio $\rho = r_p/r_s = \tan(\Psi) \exp(i\Delta)$, where r_p and r_s are the reflection coefficients for light polarized parallel and perpendicular to the plane of incidence and Ψ and Δ are the standard ellipsometric parameters.^[41] By modeling the obtained values for Ψ and Δ , a best-fit parameterized description of the dielectric function can be achieved, including optical anisotropy.^[42] IRSE measurements at different angles of incidence were performed with a Woollam IR-VASE ellipsometer. The modeling was done using the WVASE-32 software package, which appropriately considers the layered structure of the samples. The anisotropic dielectric function can then provide information on crystal orientation and structural disorder of the film.^[43] For polycrystalline thin films and amorphous films with a substrate-induced preferred orientation of the molecules, an effective uniaxial anisotropy can be expected with vibrations parallel (in-plane) and perpendicular (out-of-plane) to the substrate surface,^[44] even if the single molecules are orientated with an angle off the surface normal.

To obtain the orientation of the molecules with regard to the substrate, the experimentally observed vibrational modes were compared to density functional theory (DFT) calculations (SV(P)/BP86 level of theory)^[45] of vibrational eigenvalues and eigenvectors for a single molecule; DFT yields peak positions of vibrational modes and the directions of dipole moments relative to the molecule for each normal mode. Further information on the calculation of vibrational frequencies can be found in the Supporting Information. We developed a software tool that optimizes the accordance between DFT based vibration spectra and the experimental anisotropic dielectric function by varying the orientation of a molecule relative to the substrate.^[46] In that way, by combining DFT results, which give us the orientation of the dipole moments with respect to the molecule, and ellipsometry results, which give us the orientation of the dipole moments with respect to the substrate surface, we can reliably determine the orientation of the molecules with respect to the substrate surface.

Supporting Information

Supporting Information is available from the Wiley Online Library or from the author.

Acknowledgements

The authors would like to thank the BMBF for financial support of the OPEG project within the program on Organic Photovoltaics. The authors from the Heidelberg University acknowledge financial support via the POLYTOS project of the Leading-Edge Cluster Forum Organic Electronics within the High-Tech Strategy for Germany of the Federal Ministry of Education and Research. A.F. and C.L. acknowledge financial support from the European Commission Seventh Framework Programme (FP7/2007-2013) under Grant Agreement number 228424 Project MINOTOR. T.K. acknowledges support by an Imperial College Junior Research Fellowship. The authors would like to thank Katja Graf (BASF SE) for the AFM measurements.

Received: July 22, 2011

Published online: October 31, 2011

- [1] a) C. J. Brabec, S. Gowrisanker, J. J. M. Halls, D. Laird, S. Jia, S. P. Williams, *Adv. Mater.* **2010**, *22*, 3839; b) M. A. Green, K. Emery, Y. Hishikawa, W. Warta, *Prog. Photovolt. Res. Appl.* **2010**, *18*, 144; c) P.-L. T. Boudreault, A. Najari, M. Leclerc, *Chem. Mater.* **2011**, *23*, 456.
- [2] P. K. Nayak, J. Bisquert, D. Cahen, *Adv. Mater.* **2011**, *23*, 2870.
- [3] a) D. Veldman, S. C. J. Meskers, R. A. J. Janssen, *Adv. Funct. Mater.* **2009**, *19*, 1; b) H. Ohkita, S. Cook, Y. Astuti, W. Duffy, S. Tierney, W. Zhang, M. Heeney, I. McCulloch, J. Nelson, D. D. C. Brandley, J. R. Durrant, *J. Am. Chem. Soc.* **2008**, *130*, 3030; c) R. A. Marsh, J. M. Hodgkiss, R. H. Friend, *Adv. Mater.* **2010**, *22*, 3672; d) P. Peumans, S. R. Forrest, *Chem. Phys. Lett.* **2004**, *398*, 27.
- [4] I. G. Hill, A. Kahn, Z. G. Soos, R. A. Paskal, *Chem. Phys. Lett.* **2000**, *327*, 181.
- [5] a) D. Veldman, O. Ipek, S. C. J. Meskers, J. Sweelssen, M. M. Koetse, S. C. Veenstra, J. M. Kroon, S. S. van Bavel, J. Loos, R. A. J. Janssen, *J. Am. Chem. Soc.* **2008**, *130*, 7721; b) V. D. Mihailetschi, L. J. A. Koster, J. C. Hummelen, P. W. M. Blom, *Phys. Rev. Lett.* **2004**, *93*, 216601.
- [6] a) S. Kalyan, T. Kesti, M. Maiti, F. Zhang, O. Inganäs, S. Hellström, M. R. Andersson, F. Oswald, F. Langa, T. Österman, T. Pascher, A. Yartsev, V. Sundström, *J. Am. Chem. Soc.* **2010**, *132*, 12440; b) J.-L. Bredas, D. Beljonne, V. Coropceanu, J. Cornil, *Chem. Rev.* **2004**, *104*, 4971.
- [7] a) M. C. Scharber, D. Mühlbacher, M. Koppe, P. Denk, C. Waldauf, A. J. Heeger, C. J. Brabec, *Adv. Mater.* **2006**, *18*, 789; b) B. P. Rand, D. P. Burk, S. R. Forrest, *Phys. Rev. B* **2007**, *75*, 115327; c) C. J. Brabec, A. C. Cravino, D. Meissner, N. S. Sariciftci, T. Fromherz, M. T. Rispens, L. Sanchez, J. C. Hummelen, *Adv. Funct. Mater.* **2001**, *11*, 374; d) C. Uhrich, D. Wynands, S. Olthof, M. K. Riede, K. Leo, S. Sonntag, B. Maennig, M. Pfeiffer, *J. Appl. Phys.* **2008**, *104*, 043107.
- [8] B. C. Thompson, J. M. J. Fréchet, *Angew. Chem. Int. Ed.* **2008**, *47*, 58.
- [9] C. Uhrich, R. Schüppel, A. Petrich, M. Pfeiffer, K. Leo, E. Brier, P. Kilickiran, P. Bäuerle, *Adv. Funct. Mater.* **2007**, *17*, 2991.
- [10] X. Gong, M. Tong, F. G. Brunetti, J. Seo, Y. Sun, D. Moses, F. Wudl, A. J. Heeger, *Adv. Mater.* **2011**, *23*, 2272.
- [11] a) W. Tress, A. Petrich, M. Hummert, M. Hein, K. Leo, M. Riede, *Appl. Phys. Lett.* **2011**, *98*, 063301; b) D. Kekuda, J.-H. Huang, K.-C. Ho, C.-W. Chu, *J. Phys. Chem. C* **2010**, *14*, 2764.
- [12] a) A. Liu, S. Zhao, S.-B. Rim, J. Wu, M. Könnemann, P. Erk, P. Peumans, *Adv. Mater.* **2008**, *20*, 1065; b) J. Wagner, M. Gruber, A. Hinderhofer, A. Wilke, B. Bröker, J. Frisch, P. Amsalem, A. Vollmer, A. Opitz, N. Koch, F. Schreiber, W. Brütting, *Adv. Funct. Mater.* **2010**, *20*, 4295.
- [13] J. C. Wang, X. C. Ren, S. Q. Shi, C. W. Leung, P. K. L. Chan, *Org. Electron.* **2011**, *12*, 880.
- [14] M. Chikamatsu, T. Taima, Y. Yoshida, K. Saito, K. Yase, *Appl. Phys. Lett.* **2004**, *84*, 127.
- [15] S. Verlaak, D. Beljonne, D. Cheyns, C. Rolin, M. Linares, F. Castet, J. Cornil, P. Heremans, *Adv. Funct. Mater.* **2009**, *19*, 3809.
- [16] C. F. N. Marchiori, M. Koehler, *Synth. Met.* **2010**, *160*, 643.
- [17] R. D. Pensack, K. M. Banyas, L. W. Barbour, M. Hegadorn, J. B. Asbury, *Phys. Chem. Chem. Phys.* **2009**, *11*, 2575.
- [18] a) V. I. Arkhipov, P. Heremans, H. Bässler, *Appl. Phys. Lett.* **2003**, *82*, 4605; b) N. Koch, *ChemPhysChem* **2007**, *8*, 1438; c) G. Heimel, I. Salzmann, S. Duhm, N. Koch, *Chem. Mater.* **2011**, *23*, 359.
- [19] a) F. Würthner, K. Meerholz, *Chem. Eur. J.* **2010**, *16*, 9366; b) N. M. Kronenberg, V. Steinmann, H. Bürckstümmer, J. Hwang, D. Hertel, F. Würthner, K. Meerholz, *Adv. Mater.* **2010**, *22*, 4193; c) N. Kronenberg, M. Deppisch, F. Würthner, H. W. A. Lademann, K. Deing, K. Meerholz, *Chem. Commun.* **2008**, 6489; d) V. Steinmann, N. M. Kronenberg, M. R. Lenze, S. M. Graf, D. Hertel, K. Meerholz, H. Bürckstümmer, E. V. Tulyakova, F. Würthner, *Adv. Energy Mater.* **2011**, *1*, 888.
- [20] a) M. Brumbach, D. Placencia, N. R. Armstrong, *J. Phys. Chem. C* **2008**, *112*, 3142; b) Y. Tanaka, K. Kanai, Y. Ouchi, K. Seki, *Chem. Phys. Lett.* **2007**, *441*, 63.
- [21] a) R. W. Lof, M. A. Vanveenendaal, B. Koopmans, H. T. Jonkman, G. A. Sawatzky, *Phys. Rev. Lett.* **1992**, *68*, 3924; b) Z.-L. Guan, J. B. Kim, H. Wang, C. Jaye, D. A. Fischer, Y.-L. Loo, A. Kahn, *Org. Electron.* **2010**, *11*, 1779; c) K. Kanai, K. Akaike, K. Koyasu, K. Sakai, T. Nishi, Y. Kamizuru, T. Nishi, Y. Ouchi, K. Seki, *Appl. Phys. A* **2009**, *95*, 309.
- [22] a) M. Kröger, S. Hamwi, J. Meyer, T. Riedl, W. Kowalsky, A. Kahn, *Org. Electron.* **2009**, *10*, 932; b) M. Y. Chan, S. L. Lai, K. M. Lau, C. S. Lee, S. T. Lee, *Appl. Phys. Lett.* **2006**, *89*, 163515; c) D. R. Lide, *Handbook of Chemistry and Physics*, 75th ed. (Ed.: D. R. Lide), CRC Press, Boca Raton, USA **1995**.
- [23] a) K. Schulze, C. Uhrich, R. Schüppel, K. Leo, M. Pfeiffer, E. Brier, E. Reinold, P. Bäuerle, *Adv. Mater.* **2006**, *18*, 2872; b) H.-W. Lin, L.-Y. Lin, Y.-H. Chen, C.-W. Chen, Y.-T. Lin, S.-W. Chiu, K.-T. Wong, *Chem. Commun.* **2011**, 47, 7872.
- [24] B. W. D'Andrade, S. R. Forrest, A. B. Chwang, *Appl. Phys. Lett.* **2003**, *19*, 3858.
- [25] V. D. Mihailetschi, J. Wildeman, P. W. M. Blom, *Phys. Rev. Lett.* **2005**, *94*, 1.
- [26] B. P. Rand, J. Xue, S. Uchida, S. R. Forrest, *J. Appl. Phys.* **2005**, *98*, 124902.
- [27] C. L. Braun, *J. Chem. Phys.* **1984**, *80*, 4157.
- [28] A. Petersen, A. Ojala, T. Kirchartz, T. A. Wagner, F. Würthner, U. Rau, unpublished.
- [29] K. Hinrichs, S. D. Silaghi, C. Cobet, N. Esser, D. R. T. Zahn, *Phys. Status Solidi B* **2005**, *242*, 2681.
- [30] F. Weigend, R. Ahlrichs, *Phys. Chem. Chem. Phys.* **2007**, *7*, 3297.
- [31] S. Beckmann, K.-H. Etzbach, P. Krämer, K. Lukaszuk, R. Matschiner, A. J. Schmidt, P. Schuhmacher, R. Sens, G. Seybold, R. Wortmann, F. Würthner, *Adv. Mater.* **1999**, *11*, 536.
- [32] S. L. Mayo, B. D. Olafson, W. A. Goddard, *J. Phys. Chem.* **1990**, *94*, 8897.
- [33] a) R. A. Marcus, *J. Chem. Phys.* **1956**, *24*, 966; b) R. A. Marcus, *J. Chem. Phys.* **1957**, *26*, 872.
- [34] Y. Yi, V. Coropceanu, J.-L. Brédas, *J. Mater. Chem.* **2011**, *21*, 1479.
- [35] a) Y. Ooyama, Y. Shimada, S. Inoue, T. Nagano, T. Fujikawa, K. Komaguchi, I. Imae, Y. Harima, *New J. Chem.* **2011**, *35*, 111; b) Y. Ooyama, Y. Shimada, Y. Kawaga, Y. Yamada, I. Imae, K. Komaguchi, Y. Harima, *J. Photochem. Photobiol. A* **2009**, *203*, 177;

- c) Y. Hao, X. Yang, J. Cong, H. Tian, A. Hagfeldt, L. Sun, *Chem. Commun.* **2009**, 4031.
- [36] B. Walker, C. Kim, T.-Q. Nguyen, *Chem. Mater.* **2011**, 23, 470.
- [37] G. Wei, S. Wang, K. Sun, M. E. Thompson, S. R. Forrest, *Adv. Energy Mater.* **2011**, 2, 184.
- [38] R. Fitzner, E. Reinold, A. Mishra, E. Mena-Osteritz, H. Ziehlke, M. Pfeiffer, P. Bäuerle, *Adv. Funct. Mater.* **2011**, 21, 897.
- [39] A. J. Fry, in *Laboratory Techniques in Electroanalytical Chemistry*, (Eds.: P. Kissinger, W. R. Heineman), Marcel Dekker Ltd, New York, USA **1996**, p. 481.
- [40] a) SHELXTL program package, V. 6.14, Bruker-AXS, **2000**;
b) G. M. Sheldrick, *Acta Cryst.* **2008**, A64, 112.
- [41] R. M. A. Azzam, N. M. Bashara, *Ellipsometry and Polarized Light*, North-Holland, Amsterdam, The Netherlands **1987**.
- [42] M. Schubert, *Infrared Ellipsometry on Semiconductor Layer Structures; Springer Tracts in Modern Physics*, (Ed.: G. Höhler), Springer-Verlag, Berlin, Germany **2005**.
- [43] M. Schubert, T. E. Tiwald, C. M. Herzinger, *Phys. Rev. B* **2000**, 61, 8187.
- [44] M. Schubert, C. Bundesmann, G. Jacopic, H. Maresch, H. Arwin, *Appl. Phys. Lett.* **2004**, 84, 200.
- [45] a) J. P. Perdew, *Phys. Rev. B* **1986**, 33, 8822; b) A. D. Becke, *Phys. Rev. A* **1988**, 38, 3098.
- [46] R. Lovrincic, J. Trollmann, C. Pölking, A. Pucci, unpublished.